Penetrating Radiography of Imploding and Stagnating Beryllium Liners on the *Z* Accelerator

R. D. McBride,[1] S. A. Slutz,[1] C. A. Jennings,[1] D. B. Sinars,[1] M. E. Cuneo,[1] M. C. Herrmann,[1] R. W. Lemke,[1] M. R. Martin,[1] R. A. Vesey,[1] K. J. Peterson,[1] A. B. Sefkow,[1] C. Nakhleh,[1] B. E. Blue,[2] K. Killebrew,[2] D. Schroen,[2] T. J. Rogers,[1] A. Laspe,[1] M. R. Lopez,[1] I. C. Smith,[1] B. W. Atherton,[1] M. Savage,[1] W. A. Stygar,[1] and J. L. Porter[1]

[1]*Sandia National Laboratories, Albuquerque, New Mexico 87185, USA*

[2]*General Atomics, San Diego, California 92121, USA*

(Received 14 May 2012; revised manuscript received 11 September 2012; published 28 September 2012)

The implosions of initially solid beryllium liners (tubes) have been imaged with penetrating radiography through to stagnation. These novel radiographic data reveal a high degree of azimuthal correlation in the evolving magneto-Rayleigh-Taylor structure at times just prior to (and during) stagnation, providing stringent constraints on the simulation tools used by the broader high energy density physics and inertial confinement fusion communities. To emphasize this point, comparisons to 2D and 3D radiation magnetohydrodynamics simulations are also presented. Both agreement and substantial disagreement have been found, depending on how the liner's initial outer surface finish was modeled. The various models tested, and the physical implications of these models are discussed. These comparisons exemplify the importance of the experimental data obtained.

DOI: 10.1103/PhysRevLett.109.135004 PACS numbers: 52.58.Lq, 84.70.+p

Magnetized liner inertial fusion (MagLIF) [1,2] is a concept that involves using a pulsed electrical current to drive the implosion of an initially solid, cylindrical metal tube (liner) filled with preheated and premagnetized fusion fuel (deuterium or deuterium-tritium). One- and two-dimensional simulations using the LASNEX radiation magnetohydrodynamics code [3] predict that if sufficient liner integrity can be maintained throughout the implosion, then significant fusion yield ($>$ 100 kJ) can be attained on the 25-MA, 100-ns *Z* accelerator [1,4,5].

Imploding z-pinch systems are, however, susceptible to the magneto-Rayleigh-Taylor (MRT) instability [6–12]. For MagLIF, the loss of liner integrity prior to stagnation could cause the concept to fail. To prevent this from happening, a thick liner with an aspect ratio (AR) of less than 10 is thought to be necessary (AR $\equiv$ initial liner outer radius/initial liner wall thickness). Simulations predict an optimum in the fusion yield when the liner AR is about 6 (see Fig. 10 in Ref. [1]); larger AR liners are more susceptible to MRT instability, while lower AR liners result in slower implosion velocities.

In this Letter, we present the first experiments designed to study a MagLIF-relevant liner implosion through to stagnation. Monochromatic (6151 $\pm$ 0.5-eV) radiography with 1-ns time resolution and 15-μm spatial resolution [13] was used to image the implosions of AR $=$ 6 beryllium (Be) liners. An overview of the experiments, including the experimental setup, is given in Fig. 1. Because the radiography diagnostic provides two images per experiment, multiple experiments were conducted to acquire additional image times. The radiography data collected are shown in Fig. 2(a). The latest (bottom) two frames captured the implosion just after the inner liner surface had stagnated on axis and while trailing liner material continued to flow into the stagnation column, compressing the column further. These radiographs were recorded on Fujifilm Imaging Plate, which responds linearly to the monochromatic, 6151-eV exposure. Each radiograph has been calibrated by zeroing and normalizing the exposure using

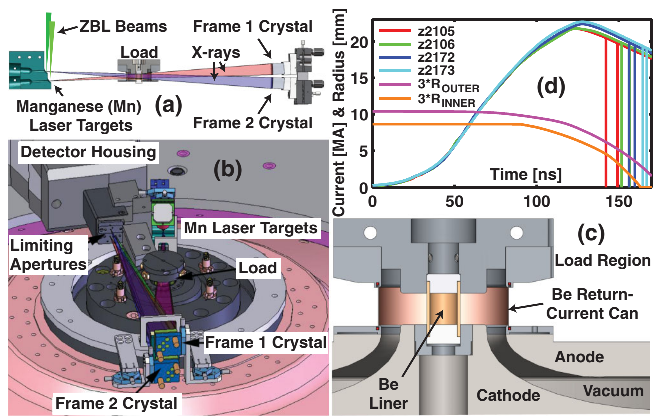

FIG. 1 (color). (a, b) Schematic illustrations of the two-frame monochromatic backlighter. The *Z* Beamlet Laser (ZBL) [14] delivers two ~1-kJ, 527-nm beams to Mn targets, generating x rays. Quartz crystals $(22\bar{4}3)$ select the 6151 $\pm$ 0.5-eV photons for imaging. (c) Half-section illustration of the load region. The 125-μm-thick, 26-mm-diameter Be return current can is approximately uniformly transparent to the 6151-eV backlighter. The minor attenuation that it causes is corrected for by the radiograph normalization and gradient-correction processes discussed in the text. (d) Drive current and radiograph times (vertical lines) from each experiment and a reference implosion trajectory from a 1D simulation that used the ALEGRA radiation magnetohydrodynamics code [15]. Each current pulse was measured by four $\dot{B}$ probes located 6 cm from the cylindrical axis of symmetry [16].

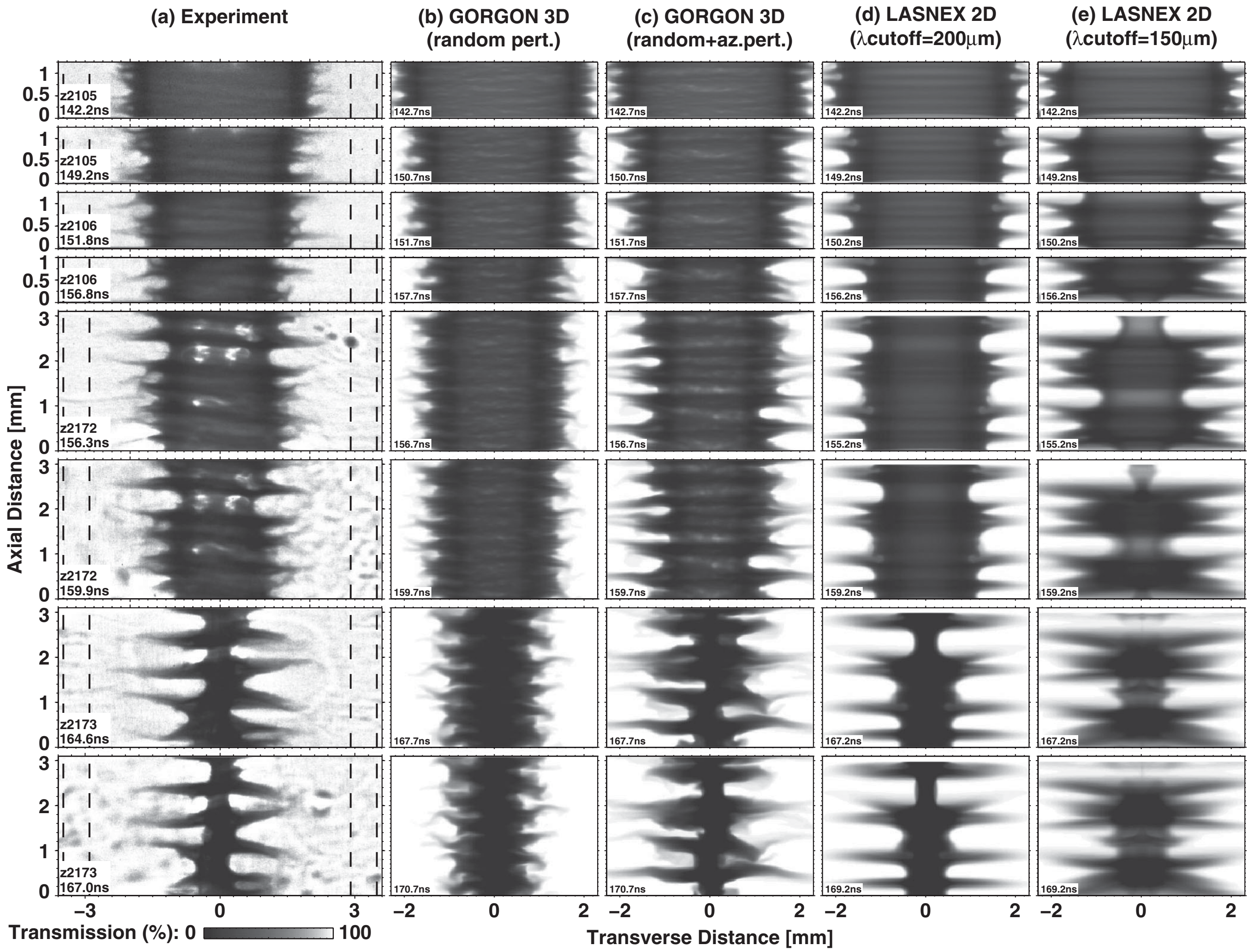

FIG. 2. (a) Radiographs from Z experiments. The vertical dashed lines indicate the initial positions of the inner and outer liner surfaces (inner and outer radii of 2.89 and 3.47 mm, respectively). (b)–(e) Synthetic radiographs from radiation magnetohydrodynamics simulations using the 3D GORGON code [17] (b),(c) and the 2D LASNEX code [3] (d),(e).

samples taken from nominally opaque regions (not shown) and nominally transparent regions (outer edges where there is no plasma), respectively. After correcting for smoothly varying gradients in exposure levels, the transmission error has been reduced to a few percent over most of each image area. In some localized regions, exposure to time-integrated self-emission from the pinch resulted in a large error (even saturating the Imaging Plate scans in some spots) [18]. Best efforts were made to avoid these regions when abstracting the various quantities presented later in this Letter.

Because of the low opacity of Be to 6151-eV photons, these radiographs reveal information about the entire volume of the imploding liner. For example, in the frames just prior to stagnation (z2172), the dark horizontal banding associated with the dominant MRT spikes shows that the MRT structure is strongly correlated azimuthally. Obtaining this level of azimuthal correlation from 3D Eulerian radiation magnetohydrodynamics simulations turned out to be nontrivial, as is illustrated in Figs. 2(b) and 2(c), where we present synthetic radiographs from a pair of simulations that used the 3D GORGON code [17]. The resolution for both of these simulations was 20 μm. The simulation in Fig. 2(b) was initialized solely with a white-noise random perturbation applied to the outer surface of the liner (i.e., cells adjacent to the liner's nominal outer surface were randomly filled with solid Be). Compared to the experiments, this simulation produced significantly less horizontal banding and azimuthal correlation. In an attempt to enhance the azimuthal correlation, and thus to better match the experiment data, the simulation in Fig. 2(c) was initialized with a bias applied to the random-surface generator at several axial locations. This bias was applied to the entire circumference of the cylinder at these locations, and each location was one cell tall. These locations were selected randomly with about 3 occurring every axial mm. This methodology is reasonable in that the surface finishes of the liners used

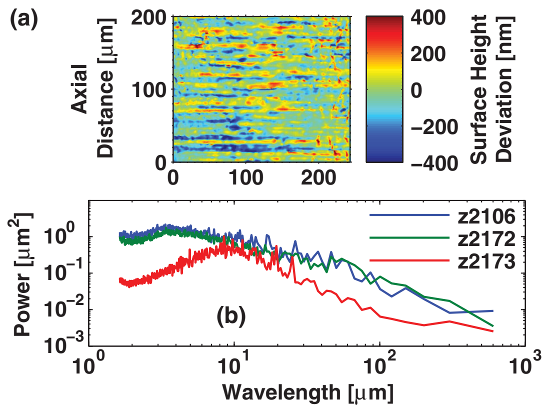

FIG. 3 (color). Liner surface finish data. (a) Sample of surface height variation illustrating azimuthally correlated structure (striations) due to the single-point, diamond-turned fabrication process (the liners were not polished or further modified). (b) Power spectra for axially aligned wave vectors (600-μm axial sample length). The liner surface finishes had a root-mean-square roughness of 100–250 nm.

for these experiments did have significant amounts of azimuthally correlated structure due to the fabrication process (see Fig. 3). This methodology attempts to capture the essence of the correlated seeding and is not intended to be a high-fidelity representation of the actual conditions.

We also ran several 2D LASNEX simulations that included a Fourier-series-constructed model of the initial liner surface that was based on a fit to the characterization data shown in Fig. 3(b). Interestingly, we found that the Fourier components with wavelengths less than about 200 μm needed to be excluded from the surface construction, or else the MRT structure would grossly overdevelop relative to the experiments [see Figs. 2(d) and 2(e)]. We are not entirely sure why this occurs. For liner implosions on much longer time scales (0–6 MA in 7 μs), Reinovsky *et al.* [9] also observed suppression of short-wavelength MRT modes, but cite solid-state liner material strength as the reason for this suppression. For the fast liner implosions presented in this Letter, however, simulations using ALEGRA, GORGON, and LASNEX all show that the liner is shock compressed and melted very early in the implosion (prior to any significant motion of the inner liner surface), and thus solid-state material strength is not believed to play a significant role in this fast-implosion case. Therefore, considering other possible explanations, one known modeling inaccuracy is that 2D simulations are by definition perfectly correlated azimuthally. In an experiment, however, the azimuthal correlation lengths of very short wavelength perturbations are small compared to the liner circumference, and thus these very short wavelength perturbations cannot contribute to the MRT development as much as that predicted by pure 2D simulations. These computational issues will be investigated and discussed further in separate publications.

To better characterize the MRT evolution of the experiments, as well as to more quantitatively compare the experiments with the simulation results shown in Figs. 2(c) and 2(d), we made use of Abel-inversion-based reconstructions of the imploding liners' volume densities. This was done by first converting both the experiment and simulation radiographs from transmission images, $T(x, z)$, to areal density images, $\rho_{\rm areal}(x, z) = -\ln T(x, z)/\kappa$, where κ is the opacity of Be to 6151-eV photons. We then Abel inverted $\rho_{\rm areal}(x, z)$ to obtain the volume density data, $\rho(R, z)$. Example volume density reconstructions are shown for the experiments in Fig. 4(a) and for the GORGON 3D simulation in Fig. 4(b). These reconstructions are not rigorous because the radiographs are not perfectly cylindrically symmetric. Furthermore, in abstracting useful quantities from these reconstructions (i.e., the plots to follow), the uncertainty is predominantly due to the nonuniformity in the MRT structure itself; this uncertainty is represented by the "error" bars plotted throughout this Letter.

Figure 4(c) displays volume density cut-through slices taken directly from the GORGON simulation output. Comparing these "true" density slice images with the Abel-reconstructed images of Fig. 4(b) illustrates the difficulty of trying to assess the integrity of the liner's inner surface from Abel-based reconstruction methods. For example, Fig. 4(c) shows that the inner surface remains reasonably well intact, while it is difficult to tell from the Abel-reconstructed images in Fig. 4(b).

To obtain a radial volume density profile for each frame, we first averaged the transmission data axially to reduce the measurement error. We then converted these axially

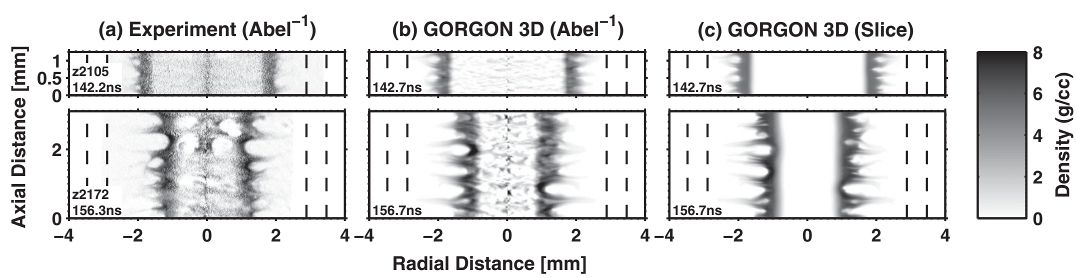

FIG. 4. Example volume density images from Z experiments (a) and GORGON 3D simulations (b),(c). The density images in (a), (b) were generated by Abel inverting the corresponding radiographs of Figs. 2(a) and 2(c). The images shown in (c) are cut-through slices taken directly from the GORGON simulation output.

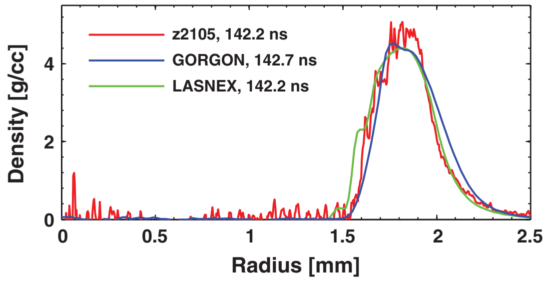

FIG. 5 (color). Example volume density profiles obtained by Abel inverting the axially averaged transmission data. The uncertainties in the experiment profiles are less than ±20%. Here the imploding liner has been compressed to about 2.5 × solid density.

averaged transmission data to areal density data, which were then Abel inverted (see examples in Fig. 5). The inner edge of each profile provided a well-localized measurement of the imploding liner's inner radius. The outer edges of these 1D profiles are, however, not very well localized due to the development of MRT structure. Thus to characterize the outer surface of each frame, we used the steep density gradients (i.e., the well-localized positions) of the dominant MRT bubbles in each volume density image. Additionally, we located the center-of-mass of the MRT spike structure that trails the bubbles. The inner, bubble, and spike radii are plotted in Fig. 6 along with reference trajectories from a 1D ALEGRA [15] simulation.

We define the MRT amplitude to be the difference between the spike radius and the bubble radius. These amplitudes are plotted in Fig. 7(a) as a function of the normalized distance that the MRT interface has moved, $1 - R(t)/R(0)$, where R is the radial position of the MRT interface and where we are using the bubble radii for $R(t)$ and the liner's initial outer radius as $R(0)$. The MRT amplitude grows nearly linearly with the distance moved. Expressed as a fraction of the distance moved, this growth is therefore nearly constant, and is in the range of 0.05–0.15, which is consistent with results from classical hydrodynamic Rayleigh-Taylor experiments in the nonlinear regime [19]. Furthermore, we find that the total mass associated with the MRT spikes also grows nearly linearly with the distance moved, and that this mass reaches a maximum of roughly 50% ± 35% of the total liner mass in the frames just before stagnation.

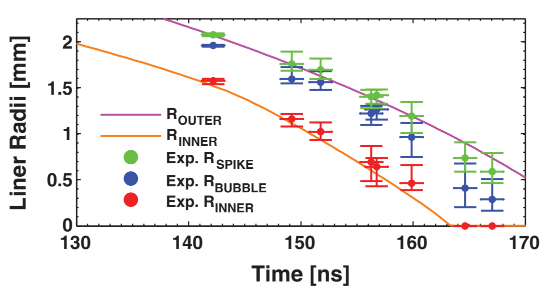

FIG. 6 (color). Inner, bubble, and spike radii (determined from the volume density reconstruction data) and reference trajectories from a 1D ALEGRA simulation. The horizontal error bars represent the ±1-ns timing uncertainty of the overall system.

From the reconstructed volume density images, we obtained $\rho R(z)|_{L,R} \equiv \int \rho(R, z) dR|_{L,R}$, where L, R indicates using the left or right side of the image data. A third series of $\rho R(z)$ data was generated using the central (on-axis) portion of the areal density images directly, i.e., $\rho_{\rm areal}(0, z) \equiv 2\rho R(z)|_C$. For each frame, these three spatial series, $\rho R(z)|_{L,R,C}$, were analyzed using a fast Fourier transform algorithm, the results of which are shown in Fig. 7(b). The wavelengths and their vertical "error" bars were determined by using the fast Fourier transform-generated power spectra as energy distribution functions. The nominal wavelength values plotted are the means of these distributions, while the vertical bars plotted bound the 50% confidence intervals of the distributions (50% of the total fluctuation energy is contained by the wavelengths within the vertical bars). The results show that

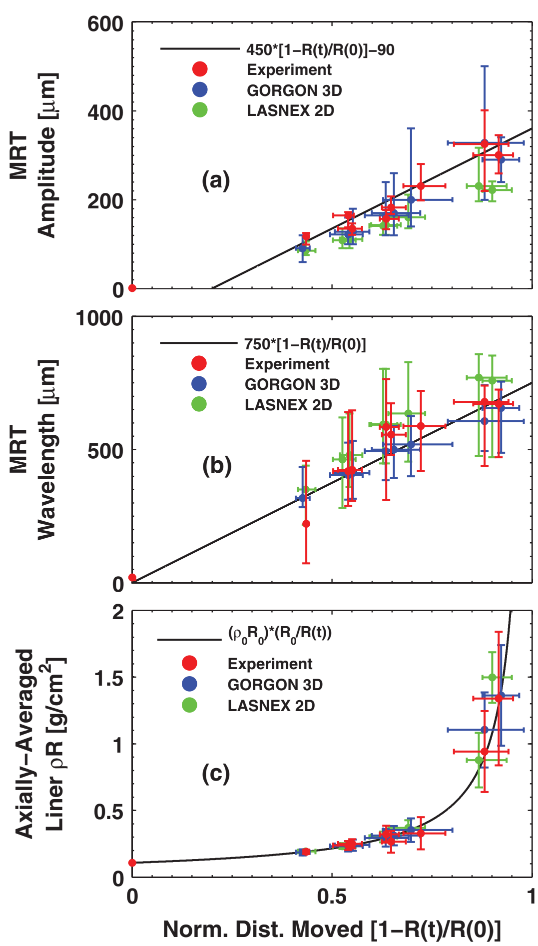

FIG. 7 (color). MRT characterization for an AR = 6 Be liner on Z. (a) MRT amplitude growth. (b) MRT wavelength growth. (c) Axially averaged liner ρR and $\Delta(\rho R)$ evolution.

the mean MRT structure grows to longer wavelengths, as has been reported elsewhere for other types of z pinches (see for example the computational studies of Ref. [20]). Like the amplitude growth, the wavelength growth is also nearly linear with distance moved.

In Fig. 7(c), we plot the results of averaging $\rho R(z)|_{L,R,C}$ over z, along with the expected liner ρR for cylindrical convergence, $(\rho_0 R_0) \times (R_0/R(t))$. The vertical "error" bars represent the uncertainty in the axially averaged liner ρR. However, they are also an indication of the imploding liners' overall $\Delta(\rho R)$ (i.e., the variation of $\rho R(z)$ along z due to the axial mass displacement associated with MRT development). The $\Delta(\rho R)$ values plotted as the vertical "error" bars were calculated using the statistical absolute deviation of $\rho R(z)$ about its mean. The axially averaged liner ρR and $\Delta(\rho R)$ are important parameters to quantify for MagLIF since this concept relies substantially on the stagnating liner mass to inertially confine the hot and dense fuel while the fusion reactions occur. Equation 20 from Ref. [1] indicates that the fusion yield should scale roughly as $(\rho R)^{1/2}$. Figure 7(c) shows that the liner $\Delta(\rho R)$ remains below about 30% of the axially averaged liner ρR at the latest time measured. Thus we might hope that the fusion yield degradation due to this level of MRT disruption remains on the order of about 16% (or less).

The authors would like to thank M. K. Matzen for programmatic support, and the Z operations, diagnostics, engineering, load hardware, and target teams for their technical assistance. This project was funded in part by Sandia's Laboratory Directed Research and Development program. Sandia National Laboratories is a multiprogram laboratory managed and operated by Sandia Corporation, a wholly owned subsidiary of Lockheed Martin Corporation, for the U.S. Department of Energy's National Nuclear Security Administration under Contract No. DE-AC04-94AL85000.

[1] S. A. Slutz, M. C. Herrmann, R. A. Vesey, A. B. Sefkow, D. B. Sinars, D. C. Rovang, K. J. Peterson, and M. E. Cuneo, Phys. Plasmas **17**, 056303 (2010).

[2] S. A. Slutz and R. A. Vesey, Phys. Rev. Lett. **108**, 025003 (2012).

[3] G. B. Zimmerman and W. L. Kruer, Comments Plasma Phys. Controlled Fusion **2**, 51 (1975).

[4] M. K. Matzen, B. W. Atherton, M. E. Cuneo, G. L. Donovan, C. A. Hall, M. Herrmann, M. L. Kiefer, R. J. Leeper, G. T. Leifeste, F. W. Long, G. R. McKee, T. A. Mehlhorn, J. L. Porter, L. X. Schneider, K. W. Struve, W. A. Stygar, and E. A. Weinbrecht, Acta Phys. Pol. A **115**, 956 (2009).

[5] D. V. Rose, D. R. Welch, E. A. Madrid, C. L. Miller, R. E. Clark, W. A. Stygar, M. E. Savage, G. A. Rochau, J. E. Bailey, T. J. Nash, M. E. Sceiford, K. W. Struve, P. A. Corcoran, and B. A. Whitney, Phys. Rev. ST Accel. Beams **13**, 010402 (2010).

[6] E. G. Harris, Phys. Fluids **5**, 1057 (1962).

[7] E. Ott, Phys. Rev. Lett. **29**, 1429 (1972).

[8] D. D. Ryutov, M. S. Derzon, and M. K. Matzen, Rev. Mod. Phys. **72**, 167 (2000).

[9] R. E. Reinovsky, W. E. Anderson, W. L. Atchison, C. E. Ekdahl, R. J. Faehl, I. R. Lindemuth, D. V. Morgan, M. Murillo, J. L. Stokes, and J. S. Shlachter, IEEE Trans. Plasma Sci. **30**, 1764 (2002).

[10] A. R. Miles, Phys. Plasmas **16**, 032702 (2009).

[11] D. B. Sinars *et al.*, Phys. Rev. Lett. **105**, 185001 (2010).

[12] D. B. Sinars *et al.*, Phys. Plasmas **18**, 056301 (2011).

[13] G. R. Bennett, I. C. Smith, J. E. Shores, D. B. Sinars, G. Robertson, B. W. Atherton, M. C. Jones, and J. L. Porter, Rev. Sci. Instrum. **79**, 10E914 (2008).

[14] P. K. Rambo, I. C. Smith, J. L. Porter, Jr., M. J. Hurst, C. S. Speas, R. G. Adams, A. J. Garcia, E. Dawson, B. D. Thurston, C. Wakefield, J. W. Kellogg, M. J. Slattery, H. C. Ives, III, R. S. Broyles, J. A. Caird, A. C. Erlandson, J. E. Murray, W. C. Behrendt, N. D. Neilsen, and J. M. Narduzzi, Appl. Opt. **44**, 2421 (2005).

[15] A. C. Robinson and C. J. Garasi, Comput. Phys. Commun. **164**, 408 (2004).

[16] T. C. Wagoner *et al.*, Phys. Rev. ST Accel. Beams **11**, 100401 (2008).

[17] J. P. Chittenden, S. V. Lebedev, C. A. Jennings, S. N. Bland, and A. Ciardi, Plasma Phys. Controlled Fusion **46**, B457 (2004).

[18] Examples of 6151-eV time-integrated self-emission can be seen in Fig. 2(a), in the two frames for z2172. They are the roughly five white amorphous regions between -1 and $+1$ mm transversely and between 1 and 3 mm axially. These five regions do not evolve from the earlier frame to the later frame of z2172 because they are caused by pinch self-emission that does not correspond to the timing (and 1-ns duration) of the x-ray backlighter.

[19] D. L. Youngs, Physica (Amsterdam) **37D**, 270 (1989).

[20] M. R. Douglas, C. Deeney, and N. F. Roderick, Phys. Plasmas **5**, 4183 (1998).